A Three-dimensional Model for the Evolution of Magnetohydrodynamic Turbulence in the Outer Heliosphere

Jens Kleimann[1,2] , Sean Oughton[3] , Horst Fichtner[1,2,4] , and Klaus Scherer[1,2,4]

[1] Institut für Theoretische Physik IV, Ruhr-Universität Bochum, 44780 Bochum, Germany; jk@tp4.rub.de
[2] Ruhr Astroparticle and Plasma Physics Center (RAPP Center), Germany
[3] Department of Mathematics, University of Waikato, Hamilton 3240, New Zealand
[4] Research Department "Plasmas with Complex Interactions", Ruhr-Universität Bochum, Germany

Abstract

We present a time-dependent, three-dimensional single-fluid model for the transport of magnetohydrodynamic (MHD) turbulence that is self-consistently evolving with a dynamic large-scale solar wind in the outer heliosphere. The emphasis is on the region beyond the termination shock, where the solar wind expands subsonically, as well as sub-Alfvénically and nonradially. In extension of earlier work, we refine the treatment of turbulence by considering, in addition to the Elsässer energies, a nonconstant energy difference (or residual energy) and by allowing each of these quantities its own characteristic correlation length scale. While the nonlinear effects in the equations for the Elsässer energies and their length scales are implemented using familiar von Kármán–Howarth style modeling of homogeneous MHD turbulence, the energy difference, which is not conserved in the absence of dissipation, and its length scale are modeled using distinct approaches. We also clarify the impact of the choice of measurement direction for correlation functions associated with two-dimensional fluctuations in transport models. Finally, we illustrate and study the solutions of the resulting six-equation model in detail.

1. Introduction

The study of turbulence in the solar wind (SW) is a topical field of contemporary heliophysical research. The ultimate goal is to establish a complete model of the heliosphere that is built on a consistent treatment of the turbulent thermal SW plasma. Important features to account for include the near-Sun acceleration of the SW, the interaction of the SW with the interstellar medium (ISM), and the transport of energetic particles within this system.

The state of the art regarding these issues has been presented in various reviews. Oughton & Engelbrecht (2021) have reviewed observations and the derived characteristics of magnetohydrodynamical (MHD) turbulence and their significance for the acceleration and transport of energetic particles. The knowledge about the intermittency of the turbulence on such fluid scales, and also on kinetic scales, has been summarized by Bruno (2019). Corresponding overviews for the turbulence properties in the heliosheath and in the local ISM can be found in Fraternale et al. (2019, 2022) and Fraternale & Pogorelov (2021). Verscharen et al. (2019) and Petrukovich et al. (2020) discussed the multiscale nature of the SW based on both in situ spacecraft measurements and theory. Concentrating on stream interactions at fluid scales, Richardson (2018) reviewed the interactions of fast and slow SW. Finally, Pogorelov et al. (2017) and Fraternale et al. (2022) surveyed the physical processes occurring in the outer heliosphere, especially at its boundary—the heliopause (HP)—which separates the inner and outer heliosheath (the IHS and OHS, respectively).

For several reasons these outer regions of the heliosphere are of high interest. First, they represent the boundary zone for the transition from SW to interstellar plasma. Second, their large-scale as well as small-scale structure determines the shielding of the heliosphere from Galactic cosmic rays and from the (neutral) ISM (see, e.g., the review by Scherer et al. 2006). The renewed interest regarding this region was triggered by the in situ exploration of the IHS (i.e., between the SW termination shock and the HP) by the Voyager 1 and 2 spacecraft, which crossed the HP and entered the local ISM in 2012 and 2018, respectively.

One of the main results derived from the Voyager measurements is that in the IHS the small scales display a considerable variability and have a significant, although not usually dominant, compressible component (e.g., Burlaga et al. 2006; Richardson & Burlaga 2013, and references therein). An understanding of the above-mentioned shielding properties of this boundary layer requires a modeling of these compressible fluctuations. We have recently begun such modeling for the whole (upwind) IHS (Fichtner et al. 2020 wherein we also reviewed previous work applied to more local regions). That work presented a transport modeling of turbulence by quasi-linearly computing the local generation of compressible fluctuations arising from the mirror instability in the IHS. The base state for the quasi-linear calculations was obtained with an MHD simulation of the large-scale interaction of the SW with the local ISM that self-consistently took into account the small-scale incompressible MHD turbulence. The study resulted in a quantification of sources of compressible turbulence in the IHS that can be included into future simulations of the turbulence transport in this region. Other models that support a systematic and quantitative simulation of the turbulence transport in the whole heliosphere, including the IHS, have also been presented. For example, Usmanov et al.

(2016) used a multifluid approach, but in terms of the fluctuations this too was limited to incompressible, one-component turbulence.

Extension of the self-consistent turbulence modeling to include the transport of compressible fluctuations from the upstream region of the termination shock (TS) into and throughout the IHS requires one more preparatory step, which we execute with the present work. This step consists in improving the modeling such that it fulfills three requirements. First, a "realistic" transport of turbulence from the supersonic to the subsonic side of the SW requires a three-dimensional (3D) model that takes the large-scale asymmetry of the IHS into account. Second, the small-scale fluid turbulence and the large-scale SW should evolve together self-consistently. Third, the turbulence model should be sophisticated enough to support necessary variation in the followed turbulence quantities. We have in mind, for example, that approximations that are well-motivated in much of the supersonic SW (upstream of the TS) may not be appropriate in the subsonic IHS, e.g., σ_D = constant (see next paragraph).

While the first two requirements were fulfilled in Usmanov et al. (2016) and Fichtner et al. (2020), both studies used simplified turbulence transport equations. In particular, they neglected the transport of compressible fluctuations[5] and required that the incompressible fluctuations are everywhere characterized by a constant normalized energy difference (σ_D) between velocity and magnetic field fluctuations, an often-made assumption (e.g., Breech et al. 2008; Usmanov et al. 2011, 2016; Engelbrecht & Burger 2013; Wiengarten et al. 2015). However, Adhikari et al. (2015, 2017) demonstrated that σ_D changes considerably with heliocentric distance, using observational data and a steady-state one-dimensional (1D) radial model based on a theory developed by Zank et al. (2012a). Moreover, using a similar modeling approach Shiota et al. (2017) found that latitudinal variations of σ_D also occur. So at present there exists no model that simultaneously fulfills all three requirements. This is the motivation for the present work. In the ensuing sections we will formulate a set of six time-dependent 3D model equations for the incompressible turbulence and solve them self-consistently with standard large-scale single-fluid MHD equations for a dynamic 3D SW.

It should be noted that, of course, further improvements could be made. First of all, the compressive fluctuations have to be added, for example, as in Zank et al. (2012b). While this is not expected to cause major technical difficulties, the exact form of a transport equation for these—valid in both the supersonic SW and the IHS—and the subtleties of the related phenomenology need thorough study, so that we reserve this extension for future investigation. Another improvement would be the consideration of a two-component model of the MHD fluctuations, with the components being turbulence and waves, roughly speaking. There are distinct types of such models (Oughton et al. 2006, 2011; Zank et al. 2017), and they have been employed as part of large-scale models of the heliosphere (Wiengarten et al. 2016; Adhikari et al. 2017). As the explicit addition of a second, wavelike component appears to be straightforward, this is, for simplicity, not yet included here. Another enhancement would concern a multifluid approach as in Usmanov et al. (2016), which could support additional physics such as the charge-exchange-induced deceleration of

---

[5] Fichtner et al. (2020) considered the local generation of compressible fluctuations but not their transport.

the solar wind. Such multifluid modeling would, of course, complicate the simulations but is, fortunately, also not essential for our purpose of studying turbulence transport in the outer heliosphere. As we show below with a validating comparison between the Usmanov et al. (2016) results and those obtained with a one-fluid model, even with the latter a rather reasonable large-scale structure of the heliosphere can be computed.

The paper is organized as follows. After a justification of the one-fluid modeling and a general description of our computational approach in Section 2, we will describe our turbulence model in Section 3, and then present and discuss simulation results in Section 4. The paper concludes with a summarizing Section 5 and two somewhat technical appendices.

2. Validation of One-fluid Modeling

For the study of compressible fluctuations in the IHS one needs to have a "realistic" large-scale structure of the heliosphere. This can be achieved, in principle, with multifluid modeling as demonstrated by Alexashov & Izmodenov (2005). Such models, already intricate, become even more cumbersome when adding equations describing the small-scale MHD turbulence (Usmanov et al. 2016). In order to demonstrate that a one-fluid model can describe the large-scale structure with sufficient accuracy, we keep the model at this stage as simple as possible but as complex as needed and base it on the one-fluid description used earlier (Usmanov et al. 2011; Wiengarten et al. 2015; see also Breech et al. (2008) and Zank et al. (2012a)).

2.1. Large-scale Equations for the Solar Wind

Our applied methodology is based on the frequently used concept of Reynolds decomposition, wherein the MHD fields are written as the sum of background (large-scale) fields and zero-mean fluctuation (primarily small-scale) fields, with the former obtained by applying a suitable averaging operator to the relevant total fields (e.g., Usmanov et al. 2011). This way, for example, we distinguish the large-scale velocity $\boldsymbol{U}$ and the fluctuation velocity $\boldsymbol{v}$.

With this approach two coupled sets of evolution equations are obtained, one for the large-scale fields and another for the fluctuation fields. The former are quite similar to the original MHD equations for the total fields, but contain additional "source" terms dependent on the fluctuations. Using a mostly familiar notation the equations for the large-scale quantities read (e.g., Usmanov et al. 2011; Wiengarten et al. 2015):

$$\partial_t \rho + \nabla \cdot (\rho \boldsymbol{U}) = 0, \tag{1}$$

$$\partial_t(\rho \boldsymbol{U}) + \nabla \cdot \left[\rho \boldsymbol{U}\boldsymbol{U} + \left(p + p_{\text{fluct}} + \frac{|\boldsymbol{B}|^2}{8\pi} \right)\mathbb{1} \right. \\ \left. - \frac{\eta}{4\pi}\boldsymbol{B}\boldsymbol{B} \right] = -\rho \boldsymbol{g}, \tag{2}$$

$$\partial_t e + \nabla \cdot \left[e\boldsymbol{U} + \left(p + \frac{|\boldsymbol{B}|^2}{8\pi} \right)\boldsymbol{U} - (\boldsymbol{U} \cdot \boldsymbol{B})\frac{\boldsymbol{B}}{4\pi} \right. \\ \left. - \frac{\rho V_A H_c}{2} \right] = -\rho \boldsymbol{U} \cdot \boldsymbol{g} - \boldsymbol{U} \cdot \nabla p_{\text{fluct}} \\ - (\boldsymbol{V}_A \cdot \nabla \rho)H_c/2 - \rho \boldsymbol{V}_A \cdot \nabla H_c \\ + \boldsymbol{U} \cdot (\boldsymbol{B} \cdot \nabla)\left[(\eta - 1)\frac{\boldsymbol{B}}{4\pi} \right] + \frac{\alpha \rho Z^3 f^+(\sigma_c)}{2\lambda}, \tag{3}$$

$$\partial_t \boldsymbol{B} + \nabla \cdot (\boldsymbol{U}\boldsymbol{B} - \boldsymbol{B}\boldsymbol{U}) = \boldsymbol{0}, \tag{4}$$

with

$$p_{\text{fluct}} = (\sigma_D + 1)\rho Z^2/4, \tag{5}$$

$$\eta = 1 + \sigma_D Z^2/(2V_A^2), \tag{6}$$

and $\mathbb{1}$ is the unit tensor. The large-scale quantities are the mass density ρ, fluid velocity $\boldsymbol{U}$, thermal pressure p, magnetic field $\boldsymbol{B}$, total energy density

$$e = \frac{\rho U^2}{2} + \frac{B^2}{8\pi} + \frac{p}{\gamma_{\text{ad}} - 1} \tag{7}$$

(with an adiabatic index $\gamma_{\text{ad}} = 5/3$), gravitational acceleration due to the Sun $\boldsymbol{g}$, and Alfvén velocity $\boldsymbol{V}_A = \boldsymbol{B}\big/\sqrt{4\pi\rho}$.

In general the large-scale fields are functions of the time t and heliocentric position vector $\boldsymbol{r}$. All computations will use the inertial frame, eliminating the need for fictitious source terms.

Equations (1)–(7) are not closed, with p_{fluct} and η functions of the fluctuating velocity $\boldsymbol{v}$ and fluctuating magnetic field $\boldsymbol{b}$. Herein we do not attempt to solve for the fluctuation *fields*, working instead with (some of) their *moments*. In particular, the fluctuations are characterized using (twice) their energy density $Z^2 = \langle v^2 + b^2 \rangle$, the cross helicity $H_c = 2\langle \boldsymbol{v} \cdot \boldsymbol{b} \rangle$, the energy difference (aka residual energy) $D = \langle v^2 - b^2 \rangle$, and a turbulence length scale λ. Here $\boldsymbol{b}$ is in Alfvén units (i.e., normalized by $\sqrt{4\pi\rho}$) and $\langle \cdots \rangle$ indicates averaging over a local region around a large-scale position $\boldsymbol{r}$. Several associated quantities are also of relevance: $\sigma_c = H_c/Z^2$ the normalized cross helicity, $\sigma_D = D/Z^2$ the normalized energy difference, the Elsässer energies $Z^2_\pm = Z^2 \pm H_c = (1 \pm \sigma_c)Z^2$, and

$$f^\pm(\sigma_c) := \frac{\sqrt{1 - \sigma_c^2}}{2}[\sqrt{1 + \sigma_c} \pm \sqrt{1 - \sigma_c}]$$
$$= \frac{Z_+^2 Z_- \pm Z_-^2 Z_+}{2Z^3}. \tag{8}$$

In the SW–ISM interaction region in particular, extracting plasma pressure from the energy density (Equation (7)) typically involves the subtraction of two large numbers to obtain a comparatively small one, which, due to the approximative nature of the numerical procedure, may easily lead to pressure becoming negative, at which point the simulation would have to abort. Therefore, we follow the procedure recommended by Balsara & Spicer (1999) and alternatively compute the pressure by integrating the entropy density $s = p/\rho^{\gamma_{\text{ad}}-1}$ via

$$\partial_t s + \nabla \cdot (s\,\boldsymbol{U}) = 0, \tag{9}$$

as a fallback option whenever pressure/temperature could otherwise become negative. Note that this procedure is not employed near shocks as entropy tends to increase across them. In practice we find that the regions of (potentially) negative pressure are almost exclusively encountered during the convergence phase, with very few such regions present in the final equilibrium state.

Additionally, a passive scalar tracer Ψ, initialized as $\Psi = -1$ in the SW region and $\Psi = +1$ in the ISM region, is integrated via

$$\partial_t(\rho\Psi) + \nabla \cdot (\rho\Psi\,\boldsymbol{U}) = 0. \tag{10}$$

This allows us to unambiguously map any fluid element to its origin, and in particular to identify the HP as the surface where $\Psi = 0$ without having to rely on isocontours of other quantities such as temperature.

2.2. Transport Equations for the Turbulence Quantities

The evolution of the small-scale MHD turbulence is obtained using an energy-containing range model (Matthaeus et al. 1994; Zank et al. 2012a). In this case, three quantities characterizing the turbulence—energy (Z^2), cross helicity (H_c), and a correlation length (λ)—are followed (Matthaeus et al. 2004; Breech et al. 2008; Usmanov et al. 2011), and we use a form that retains $O(V_A)$ terms (see Zank et al. 2012a; Usmanov et al. 2014; Wiengarten et al. 2015):

$$\partial_t Z^2 + \nabla \cdot (\boldsymbol{U}Z^2 + \boldsymbol{V}_A H_c)$$
$$= \frac{Z^2}{2}\nabla \cdot \boldsymbol{U} + 2\boldsymbol{V}_A \cdot \nabla H_c - Z^2\sigma_D\left[\frac{\nabla \boldsymbol{U}}{2} - \Gamma(\boldsymbol{U})\right]$$
$$\quad - \frac{\alpha Z^3 f^+(\sigma_c)}{\lambda} + \dot{E}_{\text{pui}}, \tag{11}$$

$$\partial_t H_c + \nabla \cdot (\boldsymbol{U}H_c + \boldsymbol{V}_A Z^2)$$
$$= \frac{H_c}{2}\nabla \cdot \boldsymbol{U} + 2\boldsymbol{V}_A \cdot \nabla Z^2 + Z^2\sigma_D\left[\nabla \cdot \boldsymbol{V}_A + \frac{\Gamma(\boldsymbol{B})}{\sqrt{4\pi\rho}}\right]$$
$$\quad - \frac{\alpha Z^3 f^-(\sigma_c)}{\lambda}, \tag{12}$$

$$\partial_t \lambda + \boldsymbol{U} \cdot \nabla\lambda \underbrace{-\sigma_c \boldsymbol{V}_A \cdot \nabla\lambda}_{\text{cross helicity}} \underbrace{-\lambda\sigma_D[\nabla \cdot \boldsymbol{U} - 2\Sigma(U) - \Gamma(U)]}_{\text{mixing}}$$
$$= \beta Z f^+(\sigma_c) - \frac{\beta\lambda}{\alpha Z^2}\dot{E}_{\text{pui}}, \tag{13}$$

where

$$\Gamma(\boldsymbol{X}) := \hat{\boldsymbol{e}} \cdot (\hat{\boldsymbol{e}} \cdot \nabla)\boldsymbol{X}, \quad \Sigma(\boldsymbol{X}) := \hat{\boldsymbol{n}} \cdot (\hat{\boldsymbol{n}} \cdot \nabla)\boldsymbol{X}, \tag{14}$$

and $\hat{\boldsymbol{e}} := \boldsymbol{B}/B \equiv \hat{\boldsymbol{B}}$ and $\hat{\boldsymbol{n}}$ are the unit vectors parallel and perpendicular to the magnetic field, respectively.[6]

The fluctuations have been assumed to be two-dimensional (2D) relative to $\boldsymbol{B}$, and isotropic in the 2D planes. This imposes a specific tensor structure for the correlation tensors and leads to the particular forms of the "mixing" terms (those involving σ_D) in Equations (11)–(13). Further details are available elsewhere along with consideration of a three-equation model suitable for fluctuations which are isotropic in 3D (Matthaeus et al. 1994; Breech et al. 2008); see also Section 3.

Note that the underbracketed terms in Equation (13) are absent in some earlier works. However, in principle they should be present if $O(V_A/U)$ effects are retained (first term) and the symmetries associated with 2D turbulence are accounted for (second term). See Appendix B for discussion on this.

In Section 2.4 we will validate the single-fluid model of the present section against published results from a four-fluid model (Usmanov et al. 2016) that also employs Equations (11)–(13), except *without* the two underbracketed terms in Equation (13). Hence for the comparison we will also drop those terms from the λ equation.

The order unity von Kármán–Howarth constants, α and β, help determine the strength of the nonlinear modeling and, in a homogeneous system with $\boldsymbol{U} = \boldsymbol{B} = \boldsymbol{0}$, determine a family of conservation laws: $Z^{2\beta/\alpha}\lambda = \text{constant}$ (Hossain et al. 1995;

---

[6] Herein we use $\hat{\boldsymbol{x}} := \boldsymbol{x}/|\boldsymbol{x}|$ to denote (either) a unit vector parallel to $\boldsymbol{x}$, or the unit vector pointing along a coordinate x.

Matthaeus et al. 1996; Linkmann et al. 2017; Bandyopadhyay et al. 2018, 2019).

No dynamical equation for the energy difference D is present as, for this category of models, σ_D is usually approximated as a constant, in part on the basis of SW observations (Roberts et al. 1987; Perri & Balogh 2010). In particular $\sigma_D = -1/3$ has often been used (e.g., Zank et al. 1996; Breech et al. 2008; Yokoi et al. 2008), corresponding to $\langle b^2 \rangle = 2\langle v^2 \rangle$.

Scattering of pickup ions and the associated generation of waves leads to an energy injection rate, modeled as (e.g., Williams & Zank 1994; Zank et al. 1996; Matthaeus et al. 1999; Smith et al. 2001; Isenberg et al. 2003; Usmanov et al. 2016)

$$\dot{E}_{\text{pui}} = C_{\text{ex}} V_A \, |U - U_{\text{ism}}|^2 \exp\left(-\frac{L_{\text{cav}}}{r} \frac{\Theta}{\sin\Theta}\right), \qquad (15)$$

with an ionization cavity radius of $L_{\text{cav}} = 5.6\,\text{au}$ and Θ the angle between the position vector r and the incident ISM flow U_{ism}. The fact that only the flow velocity relative to the ISM flow enters this expression ensures that no pickup ion sources exist in the pristine ISM. Here $C_{\text{ex}} := f_D\, \sigma\, n_H$ where $\sigma = 2 \times 10^{-15}\,\text{cm}^2$ is the mean charge-exchange cross section of a hydrogen atom, $n_H = 0.1\,\text{cm}^{-3}$ is the neutral hydrogen number density in the ISM, and $f_D < 1$ is a modeling parameter. An $\dot{E}_{\text{pui}}$ term also appears in the length scale Equation (13). For a homogeneous system this would ensure compliance with a conservation law for the quantity $Z^{2\beta/\alpha}\lambda$. Fuller discussion is available elsewhere (Hossain et al. 1995; Matthaeus et al. 1996; Breech et al. 2008).

Typically, support for driving by velocity shear is also included in transport models of this kind (e.g., Zank et al. 1996; Matthaeus et al. 1999; Smith et al. 2001; Breech et al. 2008; Wiengarten et al. 2015). Here, however, we neglect it in order to facilitate comparison of this one-fluid model with a four-fluid one, which also lacks shear driving (Usmanov et al. 2016).

We have written the three-equation model with evolution equations for Z^2 and H_c. The well-known connection of the energy and cross helicity with the Elsässer energies, $Z_\pm^2 = Z^2 \pm H_c$, means it is also straightforward to express it in terms of equations for the evolution of $Z_\pm^2$ (and λ).

2.3. Numerical Setup

We obtain numerical solutions using the CRONOS finite-volume MHD code (Kissmann et al. 2018), employing a spherical polar coordinate $[r, \vartheta, \varphi]$ grid with full 4π angular coverage and a radial extent $r \in [0.3, 900]$ au. As the numerical time step is limited by the Courant–Friedrichs–Lewy condition of the smallest cell, using a single grid for the entire volume would lead to unreasonably large computation times. For this reason, we first run a simulation on the inner region (typically covering $[r_{\min}, r_{\max}] = [0.3, 80]$ au in radius), which converges quickly (on the fluid crossing timescale, $U/r_{\max} \sim 0.8\,\text{yr}$) because the region is located entirely within the upstream region of the TS. Data from the final time frame is then used to interpolate all variables to the inner boundary of the second (outer) grid, which extends to the outer boundary at 900 au. In the radial directions the grid is stretched exponentially, such that the center r_i of cell i, $0 \leqslant i < N_r$, is at radius $r_0 + (r_{N_r} - r_0) f[(i + 1/2)/N_r]$, with a custom nonlinear scaling function $f(\xi) = (\mu^\xi - 1)/(\mu - 1)$, and μ a constant. This

Table 1
Parameters of the Inner and Outer Subgrids for the 3D Simulations Using the Three-equation Model (Labeled "[3]" in Column 1; see Section 2.4) and the Full Six-equation Model ("[6]"; see Section 4)

	N_r	N_ϑ	N_φ	$r_{\min}$	$r_{\max}$	μ	Δr Span
Inner [3]	300	180	1	0.3	100	20	0.05–1.09
Inner [6]	200	60	6	0.3	80	20	0.06–1.24
Outer [3]	180	60	90	80.0	1000	20	0.82–15.9
Outer [6]	200	60	90	80.0	900	20	0.66-12.8

Note. Dimensional parameters $r_{\min}$, $r_{\max}$, and Δr are in units of au.

causes the cell size to grow exponentially outward, supporting maximum resolution at small radii. In the limit $N_r \to \infty$, the ratio of largest to smallest cell size approaches $f'(1)/f'(0) = \mu$, while for $\mu \to 1$, the linear case $f(\xi) = \xi$ is recovered. Grid spacing in the ϑ and φ directions is uniform. Table 1 summarizes the specific grid parameters used for the simulations presented in this work.

At time $t = 0$, all (large-scale and turbulence) quantities $\{q_i(r)\}$ are initialized across the grid using an interpolation between their respective SW boundary values $(q_i)_{\text{sw}}$ and ISM region values $(q_i)_{\text{ism}}$ according to

$$q_i(r) = [1 - w(r)](q_i)_{\text{sw}} + w(r)(q_i)_{\text{ism}}. \qquad (16)$$

The weighting function $w(r)$ is zero for $r < 100$ au, unity for $r > 200$ au, and allows for a smooth transition in the intermediate region. The only exception is the magnetic field, which is constructed via

$$B(r) = \nabla \times ([1 - w(r)]A_{\text{sw}} + w(r)A_{\text{ism}}) \qquad (17)$$

to impose magnetic solenoidality, with

$$A_{\text{sw}} = B_1 \left[\frac{\Omega\,|\cos\vartheta|}{U}\,\frac{r - R_{\text{crit}}}{r}\,\hat{r} + \frac{1 - |\cos\vartheta|}{r\sin\vartheta}\,\hat{\varphi} \right], \qquad (18)$$

$$2A_{\text{ism}} = B_0 \times r = (zB_{0y} - yB_{0z})\,\hat{x} \\ + (xB_{0z} - zB_{0x})\,\hat{y} + (yB_{0x} - xB_{0y})\,\hat{z} \qquad (19)$$

the respective vector potentials of a dipolar Parker spiral field

$$B_{\text{sw}} = \nabla \times A_{\text{sw}} = \frac{B_1 s(\vartheta)}{r^2}\left[\hat{r} - \frac{\Omega\sin\vartheta}{U}(r - R_{\text{crit}})\,\hat{\varphi}\right] \qquad (20)$$

for the case of constant radial flux on each hemisphere and a homogeneous ISM field B_0 with Cartesian coordinates (B_{0x}, B_{0y}, B_{0z}). The function

$$s(\vartheta) = (\cos\vartheta)/|\cos\vartheta| \in \{\pm 1\} \qquad (21)$$

provides the polarity of each hemisphere, $\Omega = 2.6\,\mu\text{Hz}$ is an average value for the angular frequency of solar rotation (thereby ignoring differential rotation), and B_1 is the magnitude of B_{sw} at 1 au. These formulae are valid beyond the "critical" (Alfvén) radius R_{crit}, within which the field lines are purely radial. We take $R_{\text{crit}} = 10\,R_\odot$ (Marsch & Richter 1984), although the departure of results from the $R_{\text{crit}} = 0$ case is negligible for the present application. Note that the Parker spiral potential in Equation (18) is of considerably shorter form than the one proposed by Bieber et al. (1987) because the value of $\nabla \cdot A_{\text{sw}}$ is immaterial for the present purpose.

Table 2
Boundary Conditions at 0.3 au Used for the Validation Run Described in Section 2.4

Quantity	SW (Equator)	SW (Poles)	ISM
n [cm^{-3}]	210 (19.0)	30 (2.7)	0.1
U_r [km s^{-1}]	320	740	26.0
$\lvert B_r \rvert$ [nT]	35 (3.15)	35 (3.15)	0.2
T [10^3 K]	200	1100	6.135
Z^2 [(km s^{-1})^2]	500	11000	0.01
$\lvert \sigma_c \rvert$	0.0	0.8	0.0
λ [au]	0.013	0.030	1.0

Notes. For quantities scaling as $1/r^2$, the corresponding values at 1 au have been included in brackets to ease comparison. For U_r, an additional high-latitude gradient of 0.5 km s^{-1} per degree is applied, and σ_c changes sign across the equator such that $\sigma_c B_r < 0$ always. Furthermore, $\alpha = 0.128$ and $\beta = \alpha/2 = 0.064$.

2.4. Validation Against a Four-fluid Model

In order to verify that our one-fluid MHD model is able to yield similar results for the present context, and is thus of comparable usefulness to a more involved multifluid model, we performed 3D simulations using the three-equation model, with initial and boundary conditions approximating those used by Usmanov et al. (2016; themselves based on Usmanov et al. 2014) and summarized in Table 2. Results from this run are then compared to those presented by Usmanov et al. (2016), which is still the only 3D model considering turbulence in the entire heliosphere.

Figure 1 shows contour plots for selected large-scale ($\lvert \boldsymbol{B} \rvert$, U_r, U_ϑ) and all three small-scale quantities (Z^2, σ_c, λ) in the meridional plane ($\varphi = 0$) intersecting both the solar magnetic axis and the ISM inflow direction, alongside corresponding contours adapted from Figure 1 of Usmanov et al. (2016). While it is certainly unsurprising that several deviations are easily discernible (despite the boundary conditions being chosen to be as similar as possible), notable qualitative, and to some extent also quantitative, agreement is present. Shocks (TS and bow shock) are of similar shape and position, with "our" tailward TS being less round due to a more pronounced Mach disk. The weaker magnetic field piling up in the nose region could be related to stronger numerical diffusion due to the coarser grid employed here. Regarding the turbulence quantities, superior agreement is certainly found for Z^2, and also σ_c agrees well regarding its typical values in the heliosheath and at the bow shock.

In summary, the identified degree of similarity between our one-fluid model and the four-fluid one is clearly sufficient to support the application of our model to the present topic of modeling the turbulent structure of the IHS.

3. Six-equation Turbulence Model

The three-equation (transport of) turbulence model discussed in Section 2.2 is based on some approximations that, although well-motivated, nonetheless restrict its utility (for extensive discussion see Breech et al. 2008; Zank et al. 2012a). Of particular relevance are that it employs (i) a single characteristic length scale for all turbulence quantities, and (ii) the approximation $\sigma_D = $ constant, rather than solving a dynamic equation for the energy difference D. Here we present an extended model for the evolution of the heliospheric fluctuations, which addresses these shortcomings.

Six quantities are followed, the Elsässer energies $Z_\pm^2$ and energy difference of the fluctuations, and (effectively) a characteristic length scale for each of them. Related "six-equation" models have previously been considered, and we refer readers to those works for many details regarding the derivation of those and the present model (Matthaeus et al. 1994; Zank et al. 2012a; Adhikari et al. 2015). However, as our modeling of the nonlinearities is distinct—particularly in connection with D and its length scale—we will discuss this aspect in some detail in Section 3.2.

3.1. Correlation Length Scales

In deriving the model we have assumed that the fluctuations have 2D symmetry relative to $\boldsymbol{B}$ (and are isotropic in the planes perpendicular to $\boldsymbol{B}$), as was also done for the three-equation model. The tensor structures for the two-point correlation tensors and their integrals over lag—for example, $R_{ij}(\zeta \hat{\boldsymbol{n}}) = \langle v_i(\boldsymbol{x}) \, v_j(\boldsymbol{x} + \zeta \hat{\boldsymbol{n}}) \rangle_{\boldsymbol{x}}$ and $L_{ij}(\hat{\boldsymbol{n}}) = \int_0^\infty R_{ij}(\zeta \hat{\boldsymbol{n}}) \, \mathrm{d}\zeta$— are then known (Batchelor 1970; Matthaeus et al. 1994; Oughton et al. 1997) and have been used in the model's development.[7] Here, the direction associated with the spatial lag ζ is denoted by the unit vector $\hat{\boldsymbol{n}}$, and is chosen to satisfy $\hat{\boldsymbol{n}} \cdot \boldsymbol{B} = 0$. Imposing this fixed symmetry of the fluctuations has the advantage that no further approximations regarding the fluctuation correlation tensors are needed. In particular, we make no use of the *structural similarity* approximation (Tennekes & Lumley 1972; Zank et al. 1996, 2012a; Breech et al. 2008) that was employed in obtaining the three-equation model of Section 2.2, for example. In general, the tensor structures of the $R_{ij}(\zeta = 0)$ and the L_{ij} differ and this impacts the final form of the mixing terms (see Appendix B).

There is also a somewhat technical feature of the model concerning the equations determining the characteristic length scales, $\lambda_\pm$, λ_D. Rather than using evolution equations for these, it is convenient to instead evolve energy-weighted length scales, e.g., $L_\pm = \lambda_\pm Z_\pm^2$.

To obtain these equations, we recall that the fluctuation fields can be described using two sets of spatial coordinates: the large-scale heliocentric position vector $\boldsymbol{r}$ plus a small-scale offset from that, denoted $\boldsymbol{x}$ (Marsch & Tu 1989; Zhou & Matthaeus 1990). For example, $\boldsymbol{v} = \boldsymbol{v}(\boldsymbol{r}, \boldsymbol{x}, t)$. Here we are considering models for characteristic (aka energy-containing scale) quantities, meaning that at each $\boldsymbol{r}$ the dependence on the local small-scale coordinates is eliminated by averaging over them. Thus, as in earlier works (Matthaeus et al. 1994; Zank et al. 1996, 2012a; Breech et al. 2008), we derive equations for the evolution of

$$L_\pm(\boldsymbol{r}; \hat{\boldsymbol{n}}) = \int_0^\infty \langle \boldsymbol{z}^\pm(\boldsymbol{r}, \boldsymbol{x}) \cdot \boldsymbol{z}^\pm(\boldsymbol{r}, \boldsymbol{x} + \zeta \hat{\boldsymbol{n}}) \rangle_{\boldsymbol{x}} \, \mathrm{d}\zeta, \qquad (22)$$

and an analogously defined L_D. These are the integrals of the (traced) correlation functions of the Elsässer variables over the (small-scale) lags, ζ, for some chosen direction $\hat{\boldsymbol{n}}$ (e.g., Matthaeus et al. 1994, 1996). The actual characteristic length scales are defined as $\lambda_\pm = L_\pm / Z_\pm^2$.

---

[7] Recall that for a given turbulence symmetry the tensor structures of $R_{ij}(0)$, $R_{ij}(\zeta \hat{\boldsymbol{n}})$, and $L_{ij}(\hat{\boldsymbol{n}})$ are in general different. In particular only $R_{ij}(0)$ is likely to have the same symmetry as the fluctuations themselves. See, e.g., Batchelor (1970) and Appendix B.
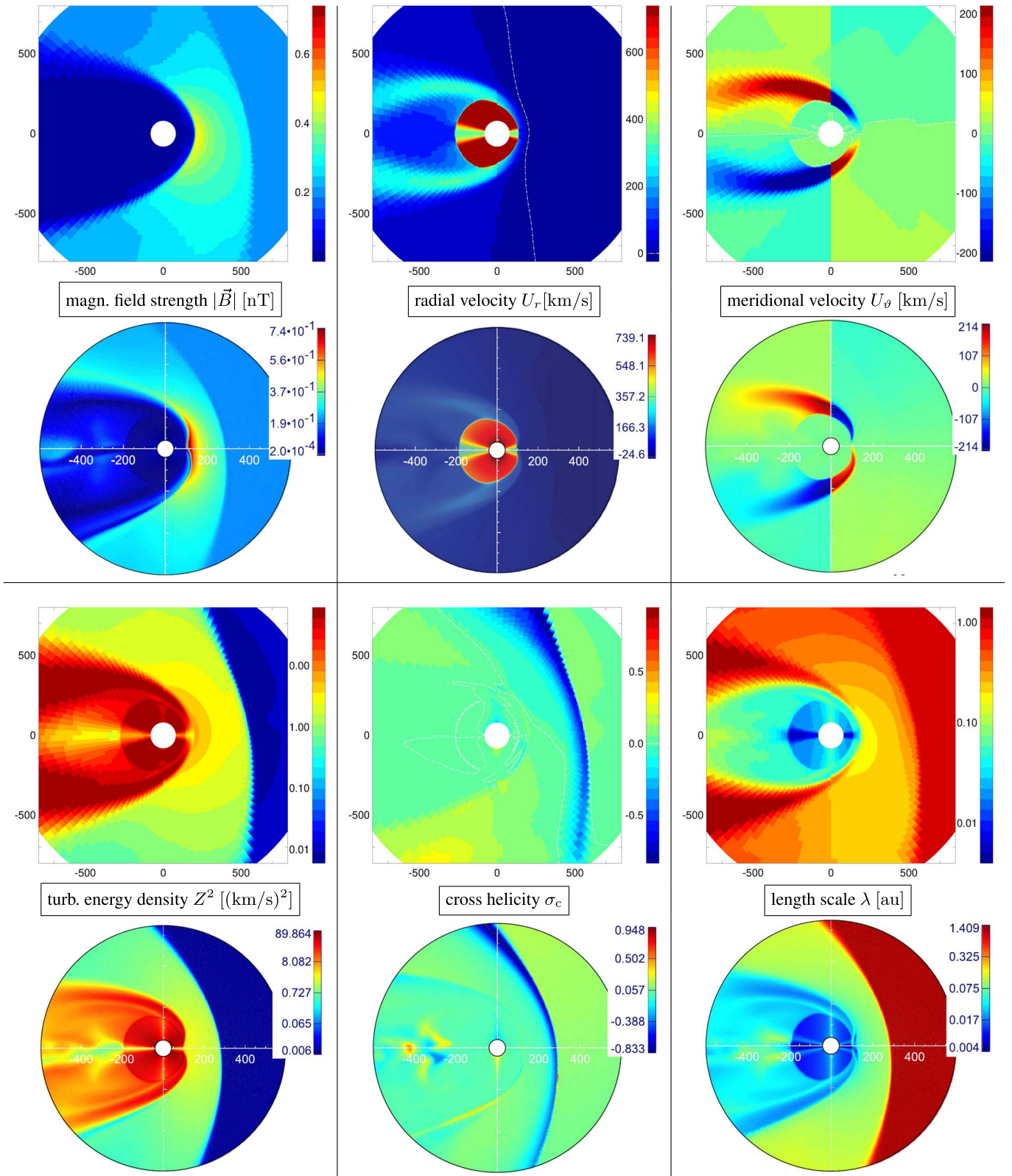
Figure 1. Meridional cuts (at $\varphi = 0$) for selected large-scale and turbulent quantities obtained using the three-equation model (rows 1 and 3), contrasted with corresponding plots adapted from Usmanov et al. (2016; rows 2 and 4). All distances are in units of au, and color tables have been adjusted to ease a qualitative comparison. Images in rows 2 and 4 courtesy of A. Usmanov.

Derivation of the transport equations themselves is straight-forward. Somewhat different models are obtained depending upon assumptions made about the turbulence properties and how modeling of the nonlinear terms should occur (e.g., Matthaeus et al. 1994, 1996; Breech et al. 2008; Zank et al. 2012a; Adhikari et al. 2015). In the present case, with 2D

symmetry for the fluctuations, the model equations are

$$\frac{\partial Z_\pm^2}{\partial t} + (\boldsymbol{U} \mp \boldsymbol{V}_A) \cdot \nabla Z_\pm^2 + Z_\pm^2 \nabla \cdot \left(\frac{\boldsymbol{U}}{2} \pm \boldsymbol{V}_A\right)$$
$$= -D\left[\nabla \cdot \left(\frac{\boldsymbol{U}}{2} \mp \boldsymbol{V}_A\right) - \Gamma(\boldsymbol{U}) \mp \frac{\Gamma(\boldsymbol{B})}{\sqrt{4\pi\rho}}\right]$$
$$- q_\pm + \dot{E}_{pui}, \tag{23}$$

$$\frac{\partial L_\pm}{\partial t} + (\boldsymbol{U} \mp \boldsymbol{V}_A) \cdot \nabla L_\pm + L_\pm \nabla \cdot \left(\frac{\boldsymbol{U}}{2} \pm \boldsymbol{V}_A\right)$$
$$= L_D\left[\nabla \cdot \left(\frac{\boldsymbol{U}}{2} \pm \boldsymbol{V}_A\right) - 2\left(\Sigma(\boldsymbol{U}) \pm \frac{\Sigma(\boldsymbol{B})}{\sqrt{4\pi\rho}}\right)\right]$$
$$+ (\beta - \alpha)Z_\pm^2 Z_\mp + \dot{E}_{pui}\lambda_\pm, \tag{24}$$

$$\frac{\partial D}{\partial t} + \boldsymbol{U} \cdot \nabla D + (D + Z^2)\nabla \cdot \left(\frac{\boldsymbol{U}}{2}\right)$$
$$= Z^2 \Gamma(\boldsymbol{U}) - H_c\left[\nabla \cdot \boldsymbol{V}_A + \frac{\Gamma(\boldsymbol{B})}{\sqrt{4\pi\rho}}\right]$$
$$- \alpha_D \frac{D}{\tau_D} - \frac{q_+ + q_-}{2}, \tag{25}$$

$$\frac{\partial L_D}{\partial t} + \boldsymbol{U} \cdot \nabla L_D + L_D \nabla \cdot \left(\frac{\boldsymbol{U}}{2}\right)$$
$$= \frac{L_+ + L_-}{2}\left[\nabla \cdot \left(\frac{\boldsymbol{U}}{2}\right) - 2\Sigma(\boldsymbol{U})\right]$$
$$- \frac{L_+ - L_-}{2}\left[\nabla \cdot \boldsymbol{V}_A - 2\frac{\Sigma(\boldsymbol{B})}{\sqrt{4\pi\rho}}\right] - \frac{L_D}{\tau_D}, \tag{26}$$

with $L_D := \lambda_D D$ encoding the third length scale[8] λ_D, and

$$q_\pm = \alpha \frac{Z_\pm^2 Z_\mp}{\lambda_\pm} \equiv \alpha \frac{Z_\pm^4 Z_\mp}{L_\pm}, \tag{27}$$

$$\tau_D = \frac{(L_+ + L_-)/(2Z^2)}{\sqrt{V_A^2 + (Z^2 - D)/2}} \equiv \frac{\lambda_Z}{V_A^{tot}}. \tag{28}$$

Here τ_D is an Alfvénic timescale based on a length scale for the energy $Z^2 = (Z_+^2 + Z_-^2)/2$, rather than the energy difference D (see Section 3.2 for discussion on this point). The dissipation of fluctuation energy (per volume) is $\rho(q_+ + q_-)/4$ and replaces the final term in the energy Equation (3), its three-equation analog. The $Z_\pm^2$ and $L_\pm$ equations include $\boldsymbol{V}_A \cdot \nabla$ terms on their respective LHS. As we regard the fluctuations as being quasi (rather than strictly) 2D this is clearly appropriate. Here quasi-2D means the fluctuations can vary weakly along the parallel ($\boldsymbol{B}_0$) direction (Matthaeus et al. 1990). We note, however, that in some Nearly Incompressible turbulence transport models (e.g., Zank et al. 2017) it is argued that, for the strictly 2D fluctuations, the $\boldsymbol{V}_A \cdot \nabla$ terms do not feature.

This six-equation model differs from many three-equation models in how the effects of pickup ion driving are included. Here the latter are restricted to just input of energy, in Equation (23), with no direct modification of the equations for

the length scales $\lambda_\pm = L_\pm/Z_\pm^2$. The physical motivation is that the pickup ion energy is injected at *parallel* length scales of order the proton gyroradius, and thus should not (directly) affect the perpendicular length scales employed in this six-equation model. So although $\dot{E}_{pui}$ terms are present in the $L_\pm = Z_\pm^2 \lambda_\pm$ equations, their role there is to ensure that when equations for $\lambda_\pm$ are extracted from Equation (24) no $\dot{E}_{pui}$ terms appear in the $\lambda_\pm$ equations. As discussed in Section 2.1, three-equation models have typically adopted a different approach, by including a (decay) term proportional to $\dot{E}_{pui}$ in the equation for λ, such as Equation (13). The forcing is then consistent with the local conservation law, $Z^{2\beta/\alpha}\lambda = $ constant. There are also other approaches. For example, transport models which track a parallel length scale, say $\lambda_\parallel$, can accommodate influence of pickup ions on the evolution of $\lambda_\parallel$ (e.g., Oughton et al. 2011).

Referring to Equation (14) for the definitions of $\Gamma(\cdot)$ and $\Sigma(\cdot)$, we see that, because $\hat{\boldsymbol{e}}\|\boldsymbol{B}$ and $\hat{\boldsymbol{n}} \perp \boldsymbol{B}$, the two identities

$$\Gamma(\boldsymbol{B})/\sqrt{4\pi\rho} = \Gamma(\boldsymbol{V}_A) - \nabla \cdot \boldsymbol{V}_A, \tag{29}$$

$$\Sigma(\boldsymbol{B})/\sqrt{4\pi\rho} = \Sigma(\boldsymbol{V}_A). \tag{30}$$

hold. These may be used to "hide" factors involving $\sqrt{4\pi\rho}$.

The special case $\lambda_+ = \lambda_- = \lambda_D (= \lambda)$ is of interest as under those conditions one would like the model to be consistent with the three-equation one of Section 2.2. Indeed, the sum and difference of Equation (23) are then formally equivalent to Equations (11) and (12). Similarly, adding Equations (24) and then extracting the equation for λ recovers Equation (13). To make the equivalence complete one discards the dynamical Equation (25) for D (and that for L_D), and uses instead the closure relation of constant $\sigma_D = D/Z^2$ (see also Appendix B.).

3.2. Modeling of Nonlinear Terms

In developing the six-equation model the nonlinear effects in the $Z_\pm^2$ and $L_\pm$ equations are implemented using familiar von Kármán–Howarth style modeling of homogeneous MHD turbulence (Matthaeus et al. 1994, 1996; Hossain et al. 1995; Zank et al. 1996, 2012a; Smith et al. 2001; Breech et al. 2008; Wan et al. 2012). These are the terms with factors of α and/or β, including Equation (27). Observational studies support such modeling of SW fluctuations (e.g., Roy et al. 2022).

The energy difference D, however, is a different sort of quantity. Unlike the $Z_\pm^2$ it is not conserved in the absence of dissipation. Hence, phenomenological modeling of the evolution of D, and L_D, usually takes a different approach with ours outlined below.

Earlier works have considered various models for the nonlinear evolution of D, at either the energy-containing level (Matthaeus et al. 1994; Yokoi 2006; Yokoi & Hamba 2007; Yokoi et al. 2008; Zank et al. 2012a; Adhikari et al. 2015) or the inertial range (spectral) level (Pouquet et al. 1976; Grappin et al. 1983, 2016; Müller & Grappin 2005). Closure-informed arguments led to the suggestion that in the inertial range

$$\frac{\partial D(k)}{\partial t} = -\frac{D(k)}{\tau_{equi}} - \frac{E(k)}{\tau_{xfer}}, \tag{31}$$

with conceptually distinct options explored for the timescales associated with return to energy equipartition (τ_{equi}) and energy transfer (τ_{xfer}; Pouquet et al. 1976; Grappin et al. 1983, 2016). Transcribing this to a (homogeneous) energy-containing range

---

[8] Clearly $L_D = \lambda_v \langle v^2 \rangle - \lambda_b \langle b^2 \rangle$ is a physically well-defined quantity that is not necessarily zero when $D = \langle v^2 - b^2 \rangle = 0$. However, the definition $\lambda_D := L_D/D$ has interpretation complications when $D = 0$.

phenomenology gives (Matthaeus et al. 1994)

$$\frac{dD}{dt} = -\alpha_D \frac{D}{\tau_D} - \frac{Z^2}{\tau_Z}, \qquad (32)$$

with α_D an $O(1)$ constant. The first term causes $|D| \to 0$, (i.e., equipartition of $\langle v^2 \rangle$ and $\langle b^2 \rangle$) on the timescale τ_D, while the (always negative) second term acts to make D smaller. The final terms in Equations (25) and (32) are equivalent provided one uses the definition

$$\tau_Z = (Z_+^2 + Z_-^2)/(q_+ + q_-), \qquad (33)$$

i.e., the timescale associated with the energy cascade rate. Recall that $Z^2 = \langle v^2 + b^2 \rangle = (Z_+^2 + Z_-^2)/2$.

An advantageous feature of this model is its prediction of a negative $\sigma_D = D/Z^2 = -\tau_D/(\alpha_D \tau_Z)$ at steady state (Grappin et al. 1983; Mangeney et al. 1991). This accords with MHD simulation results (e.g., Pouquet et al. 1976; Oughton et al. 1994, 2016; Bigot et al. 2008; Bigot & Galtier 2011) and typical solar wind observations (e.g., Perri & Balogh 2010). As the Alfvén effect (Kraichnan 1965; Pouquet et al. 1976), which involves movement of D toward zero, is likely to be active we model τ_D as an Alfvén timescale[9] as indicated in Equation (28). There, $\lambda_Z = (L_+ + L_-)/(2Z^2)$ is a characteristic length scale for the fluctuation energy $Z^2 \equiv \langle v^2 + b^2 \rangle$ and V_A^{tot} is the Alfvén speed arising from the combination of the mean magnetic field and the rms fluctuation field strength. In place of λ_Z one might have employed a length scale seemingly more directly associated with D, such as $\lambda_D = L_D/D$. However, working with λ_D can produce difficulties when $D \approx 0$, so we make the plausible assumption that D and Z^2 have similar characteristic length scales.

Consider now nonlinear effects in the evolution of L_D. Again, various models have been proposed (Matthaeus et al. 1994, 1996; Zank et al. 2012a; Dosch et al. 2013; Adhikari et al. 2015). A "kinematic" requirement is that in order for λ_v and λ_b—the correlation scales for the fluctuation velocity and magnetic field—to be positive, L_D needs to satisfy the realizability constraint $|2L_D|/(L_+ + L_-) \leqslant 1$. If the six-equation model is solved with the final term in Equation (26), namely, $Q_{L_D} := -L_D/\tau_D$, absent, this constraint is often violated with negative values of λ_v occurring. This suggests that nonlinear and/or wavelike activity reins in the magnitude of L_D and thus modeling of the associated process(es) should be included. Moreover, results from homogeneous MHD turbulence simulations (unpublished) suggest that $|L_D| \sim (L_+ + L_-)/10$ or even smaller. Our form for Q_{L_D}—that is, a phenomenologically motivated damping which acts to reduce $|L_D|$ on the same Alfvénic timescale (τ_D) present in the D equation—is an attempt to account for both of these behavioral aspects. Although some dimensional analysis and modeling approaches have suggested that a nonlinear timescale like τ_Z would be appropriate to use here (Zank et al. 2012a; Grappin et al. 2016), we have instead opted to employ an Alfvénic timescale on the basis that the Alfvén effect should influence L_D as well as D.

In developing the six-equation model it is desirable that the modeled terms obey constraints associated with the true terms. Such constraints include the realizability condition for L_D discussed in the previous paragraph and similar conditions for the positivity of the kinetic and magnetic energies

$|\sigma_D| = |D|/Z^2 \leqslant 1$, and the Elsässer energies $|\sigma_c| \leqslant 1$. Regrettably, we lack analytic demonstrations that our modeled terms will impose these restrictions. To alleviate the issue, we take a pragmatic approach. For example, we test the local magnitude of σ_c at each time step and, if necessary, reduce it. In practice such "clamping" is only required for a tiny fraction of the computational cells (see Section 4).

3.3. Selection of $\hat{n}$

Unlike $\hat{e}$, which always points along B, the perpendicular unit vector $\hat{n}$ allows for some residual freedom of free rotation around B, and this impacts the determination of $\Sigma(\cdot)$; see Equation (14). Matthaeus et al. (1994) chose $\hat{n}$ to (also) be perpendicular to $\hat{r}$, but their model is restricted to the spherically symmetric SW flow upwind of the TS, where a preference for the radial direction can be more easily motivated. For small-scale turbulence beyond the TS, however, there is nothing particularly distinct about the position of the Sun, implying that $\hat{n}$ may be chosen based on the local properties of the plasma flow. In this vein, let us introduce a parameterization

$$\hat{n} = \hat{x}' \cos\gamma + \hat{y}' \sin\gamma \qquad (34)$$

with respect to a mean-field-aligned local Cartesian coordinate system (x', y', z') with orthonormal basis vectors

$$[\hat{x}', \hat{y}', \hat{z}'] = \left[\frac{\hat{U} \times \hat{B}}{\sin\psi}, \frac{\hat{B} \times (\hat{U} \times \hat{B})}{\sin\psi}, \hat{B} \right], \qquad (35)$$

with $\sin\psi$ ensuring proper normalization of the unit vectors.[10] With respect to the above coordinates, we have

$$\Gamma(X) = \hat{z}' \cdot (\hat{z}' \cdot \nabla) X = \frac{\partial X_{z'}}{\partial z'}, \qquad (36)$$

$$\Sigma(X) = (\cos^2\gamma) \frac{\partial X_{x'}}{\partial x'} + (\sin^2\gamma) \frac{\partial X_{y'}}{\partial y'} + (\cos\gamma)(\sin\gamma) \left(\frac{\partial X_{x'}}{\partial y'} + \frac{\partial X_{y'}}{\partial x'} \right). \qquad (37)$$

This also shows explicitly that, without loss of generality, for symmetry reasons it will be sufficient to allow angle γ to vary only in the interval $[0, \pi]$.

So in general we will expect these dynamical turbulence equations, and hence also the results which they produce, to depend on γ as it varies continuously between 0 and π. In the absence of any obvious preference for a specific value of γ, we first observe that the averaging Equation (37) over γ gives

$$\langle \Sigma(X) \rangle_\gamma = \frac{1}{2} \left(\frac{\partial X_{x'}}{\partial x'} + \frac{\partial X_{y'}}{\partial y'} \right). \qquad (38)$$

Interestingly, the above expression is identical to $(1/2)[\Sigma(X)|_{\gamma=0} + \Sigma(X)|_{\gamma=\pi/2}]$, the arithmetic average of the two cases $\hat{n} = \hat{x}'$ and $\hat{n} = \hat{y}'$. Moreover, combining Equations (36) and (38) yields

$$2\langle \Sigma(X) \rangle_\gamma + \Gamma(X) = \nabla \cdot X, \qquad (39)$$

---

[9] Contrastingly, Grappin et al. (2016) suggest that (the spectral version of) τ_D should be a nonlinear timescale rather than an Alfvénic one.

[10] We can consistently use ψ, the angle between B and the generally nonradial U, both here and in Equation (40) where U is strictly radial.

which, thanks to the covariant definitions of $\Gamma(\cdot)$ and $\Sigma(\cdot)$ in Equation (14), is valid in any coordinate system. In particular is it independent of our specific choice of orthonormal basis vectors (Equation (35)).

We will retain the dependence on γ for the radial test case to be presented in Section 3.5 but otherwise use Equation (39) to replace both $\Sigma(U)$ and $\Sigma(B)$ by their γ-averaged counterparts (see Appendix A for a summary of the equations thus arrived at). As (i) only $\hat{n}$ depends on γ, and (ii) all equations that depend on $\Sigma(X)$ do so in a linear way, this is equivalent to averaging the entire set of equations with respect to γ. This averaging affords some algebraic simplification.

3.4. Equations in Conservative Form

For reasons of numerical convenience (see Section 2.3) it is advantageous to express the equations in conservative form. The large-scale equations are already so-expressed (see Section 2.1), and those forms for the turbulence quantities are readily obtained from the equations given in Sections 2.2 and 3. Appendix A lists the γ-averaged six-equation model in conservative form.

3.5. Validation Against a Steady-state Radial Version

As a simple test case to verify the correct implementation, we consider the special case of a radial ($\partial_\vartheta = 0 = \partial_\varphi$), stationary ($\partial_t = 0$) setting with a purely radial SW flow $U = U\hat{r}$ of constant magnitude U, a monopolar Parker (1958) spiral field

$$B = B_0 \left(\frac{R_{\text{crit}}}{r}\right)^2 [\hat{r} - \hat{\varphi} \tan \psi], \tag{40}$$

with

$$\tan \psi = \frac{\Omega \sin \vartheta}{U}(r - R_{\text{crit}}) \tag{41}$$

(evaluated at $\vartheta = \pi/2$) giving the winding angle ψ at which equatorial field lines meet with the radial direction. This implies

$$\nabla_i U_j = (\delta_{ij} - \hat{r}_i \hat{r}_j) U/r, \tag{42}$$

$$\nabla \cdot U = \frac{2U}{r} \quad \text{and} \quad \nabla \cdot V_A = \frac{V_{A,r}}{r}. \tag{43}$$

The turbulence Equations (23)–(26) then simplify to the following set of ordinary differential equations, after using Equations (29) and (30)

$$(U \mp V_{A,r})\frac{dZ_\pm^2}{dr} = -\frac{(U \pm V_{A,r})Z_\pm^2 + UD}{r} - q_\pm$$
$$+ [\Gamma(U) \pm \Gamma(V_A)]D + \dot{E}_{\text{pui}}, \tag{44}$$

$$(U \mp V_{A,r})\frac{dL_\pm}{dr} = -\frac{(U \pm V_{A,r})(L_\pm - L_D)}{r}$$
$$- 2L_D[\Sigma(U) \pm \Sigma(V_A)]$$
$$+ (\beta - \alpha)Z_\pm^2 Z_\mp + \dot{E}_{\text{pui}} \lambda_\pm, \tag{45}$$

$$U\frac{dD}{dr} = -\frac{U(D + Z^2)}{r} + Z^2 \Gamma(U) - H_c \Gamma(V_A)$$
$$- \alpha_D \frac{D}{\tau_D} - \frac{q_+ + q_-}{2}, \tag{46}$$

$$U\frac{dL_D}{dr} = (L_+ + L_-)\left[\frac{U}{2r} - \Sigma(U)\right] - \frac{UL_D}{r}$$
$$- (L_+ - L_-)\left[\frac{V_{A,r}}{2r} - \Sigma(V_A)\right] - \frac{L_D}{\tau_D}. \tag{47}$$

When dealing with the equations in nonconservative form, the use of $Z_\pm^2$ is preferred over $\{Z^2, H_c\}$ because Equations (44) involve only one derivative, whereas their sum and difference each involve derivatives of both Z^2 and H_c (see Equations (A1) and (A2)).

With the basis vectors in Equation (35) taking the form

$$\hat{x}' = \hat{\vartheta}, \tag{48}$$

$$\hat{y}' = (\sin \psi)\hat{r} + (\cos \psi)\hat{\varphi}, \tag{49}$$

$$\hat{B} = \hat{z}' = (\cos \psi)\hat{r} - (\sin \psi)\hat{\varphi}, \tag{50}$$

we obtain

$$\Gamma(U) = \frac{U}{r} \sin^2 \psi, \tag{51}$$

$$\Gamma(V_A) = -\frac{V_{A,r}}{r}\frac{r \cos^2 \psi - R_{\text{crit}}}{r - R_{\text{crit}}}. \tag{52}$$

Here, we refrain from using Equation (39) relating $\langle\Sigma(\cdot)\rangle_\gamma$ and $\Gamma(\cdot)$ as documented in Section 3.3, but rather retain the full dependence on γ, so that

$$\Sigma(U) = \frac{U}{r} T(\gamma), \tag{53}$$

$$\Sigma(V_A) = \frac{V_{A,r}}{r}\frac{r T(\gamma) - R_{\text{crit}}}{r - R_{\text{crit}}}, \tag{54}$$

with

$$T(\gamma): = \cos^2 \psi + \cos^2 \gamma \sin^2 \psi \tag{55}$$

and the angle γ as a free parameter. These expressions are of course consistent with Equation (39), and, as the form for $T(\gamma)$ indicates, in this special case γ only needs to vary in the interval $[0, \pi/2]$.

The steady 1D Equations (44)–(47) were solved for a range of $\hat{n}$ orientations $\gamma \in [0°, 90°]$, subject to the $r = 0.3$ au equatorial SW boundary conditions listed in Table 3, using a standard fourth-order Runge–Kutta (RK) integrator. Additionally, using the same spherically symmetric inner boundary conditions, a steady solution of the full time-dependent 3D model (with six turbulence equations) was obtained, using CRONOS. The solution was however obtained on a narrow 3D grid that only covered the beam with $\vartheta \in [0.48, 0.49]\pi$ and $\varphi \in [0, 0.02]\pi$, and all large-scale quantities artificially held fixed. For this latter simulation run, the closure relation (Equation (39)) was used to avoid having to specify γ.

Figure 2 displays the radial dependence of selected turbulence quantities, as obtained from the RK and CRONOS 1D simulations described in the previous paragraph. Clearly, the influence of $\hat{n}$'s direction, encoded in the angle γ, is rather small, except for λ_D, where it is quite substantial. As can be seen for λ_D (and also verified for the other quantities), the curves agree almost perfectly with the respective curves for $\gamma = \pi/4$, as should be the case as

$$T(\pi/4) = (1 + \cos^2 \psi)/2 = \langle T(\gamma)\rangle_\gamma. \tag{56}$$

Table 3
Inner (0.3 au) and Outer (ISM) Boundary Conditions for Both the 1D
Comparison of Section 3.5 and the Fully 3D Simulations of Section 4

Quantity	SW (Equator)	SW (Poles)	ISM
n [cm^{-3}]	55.5 (5.0)	22.2 (2.0)	0.1
U [km s^{-1}]	380	740	26.0
$\lvert B_r \rvert$ [nT]	44.4 (4.0)	44.4 (4.0)	0.2
T [10^3 K]	300	1400	6.135
Z^2 [(km s^{-1})^2]	2200	11000	0.01
$\lvert \sigma_c \rvert$	0.4	0.8	0.0
σ_D	-0.3	-0.3	0.0
λ_+ [au]	0.012	0.002	2000
λ_- [au]	0.009	0.006	2000

Note. Values are listed in analogy to Table 2. L_D is set to $L_D = -(L_+ + L_-)/10$ on the boundaries (and initially).

This agreement for this special case serves as a first test to verify proper implementation of the 3D equations. Of course the exact agreement is an artifact of the simple SW background flow and field that led to the similarly simple angular dependence of Equations (53)–(55), and cannot be expected for other situations, in which the sum of mixed derivatives in Equation (37) does not generally vanish. (We note that for a similar comparison in which the Alfvénic timescale τ_D in Equation (26) was tentatively replaced by the longer nonlinear timescale, $\tau_Z := (Z_+^2 + Z_-^2)/(q_+ + q_-)$, the variation among curves for different γ is much more pronounced.)

Although the focus of the present study is on the evolution of turbulence beyond the TS, it is useful to compare the results obtained for the supersonic solar wind (Figure 2) to available data. Such comparisons have been presented in Adhikari et al. (2015) and were later extended by Adhikari et al. (2017). These authors also confronted results of a spherically symmetric turbulence model with the observational data. We remark that the data are quite scattered and do not suggest that a single (steady-state) radial profile holds. While the radial profiles we have computed herein differ from those presented in these earlier studies, which is mainly a consequence of the differences in the turbulence modeling, they still appear to be compatible with the spacecraft data. There is a qualitative agreement regarding the increase in the correlation lengths λ_+ and λ_-, with the former being slightly larger than the latter. Furthermore, our results for the cross helicity σ_c and the residual energy σ_D appear to be consistent with the SW data shown in Figures 5 and 7 of Adhikari et al. (2015); see also Figure 1 in Adhikari et al. (2017).

In addition to its importance for code verification, the comparison shown in Figure 2 is also of direct scientific interest. For instance, it confirms that the employed equations are indeed suitable to keep both $\lvert \sigma_c \rvert$ and $\lvert \sigma_D \rvert$ below unity for any γ, at least in the supersonic SW. Moreover, we see that λ_D can become negative for $\gamma > 45°$, and that the γ-averaging approach avoids this "problem," albeit barely so. The definition of $\lambda_D = L_D/D$ indicates that it being negative is not formally an issue, as both D and L_D may be negative. However, if one wished to keep $\lambda_D > 0$, then Figure 2 suggests that the lag vector $\hat{n}$ should either be averaged over, or be selected to point in the approximate direction of $U \times B$.

## 4. 3D Simulations Using the Full Six-equation Model

Simulations of the improved six-equation turbulence model were carried out as described in Section 2.4 except that the turbulence evolution is given by Equations (A1)–(A5) rather than Equations (11)–(13). This also necessitates replacing the final term in the energy Equation (3)—which represents the dissipation of fluctuation energy—by the form associated with the six-equation model: $\rho(q_+ + q_-)/4$. Below we first describe the boundary conditions and make some remarks on a numerical issue. Simulation results are then discussed.

Figure 3 shows the variation of density, radial velocity, and temperature at the inner boundary that have been implemented to capture the slow/fast SW dichotomy and the corresponding change seen in other quantities as a function of the heliolatitude. Based on Ulysses observations (McComas et al. 2000) an additional gradient of 1 km s^{-1} per degree of heliolatitude is included for the radial velocity (see Usmanov et al. 2011). Density varies approximately according to $n(\vartheta) \propto [U_r(\vartheta)]^{-1.4}$, again in accord with Ulysses data (Pogorelov et al. 2013). This exponent represents a compromise between constant mass flux (exponent -1) and constant momentum density (exponent -2). All other quantities vary with ϑ according to the same functional form as temperature but with their own equatorial and polar values as listed in Table 3. Therein, those for Z^2, σ_c, and most of the large-scale MHD values have been adopted from Wiengarten et al. (2015), Usmanov et al. (2016), and Larrodera & Cid (2020), while those for the length scales are informed by observational analyses (Tu et al. 1989; Adhikari et al. 2015; Burlaga et al. 2018). The chosen latitudinal dependence of Z^2 is consistent with available observations (e.g., Bavassano et al. 2001; Breech et al. 2008; Chen et al. 2020). Further parameters are $f_D = 0.25$, $\alpha_D = 0.5$, $\alpha = 0.3$, and $\beta = \alpha/2 = 0.15$.

A practical problem arises for the dimensionless quantities σ_c and σ_D. On the one hand, their definitions mean that they are physically restricted to the interval $[-1, 1]$, while on the other hand there is nothing in the equations governing their evolution, Equations (A1) and (A2), to strictly enforce this property. Hence the integrator procedure was set to clamp them within the interval $[-0.98, 0.98]$ at the beginning of each integration step. Even with such clamping, the $\dot{E}_{\text{pui}}$ driving in the length scale Equations (A4) can be computationally problematic as it grows very large for $\lvert \sigma_c \rvert$ near unity. This is seen to typically occur at or close to the bow shock, see the corresponding panel in Figure 1. We have therefore disabled the $\dot{E}_{\text{pui}}$ terms beyond the HP by augmenting them with a step function factor, $H(-\Psi)$, that is zero in the ISM, where the scalar tracer $\Psi > 0$; see Equation (10). This can be justified by noting that the focus of the present paper is on the inner heliosheath, not the outer, and that these regions are separated by the impenetrable HP, whose position (and shape) are not noticeably influenced by small-scale quantities.

4.1. Simulation Results

Figure 4 shows cuts along the meridional ($\varphi = 0$) and equatorial ($\vartheta = \pi/2$) planes for the turbulence quantities Z^2, $\lambda_\pm$, L_D, σ_c, and σ_D after convergence to a steady-state is attained. Together with the analytical formulation of the six-equation model itself, this figure represents the central result of our study.
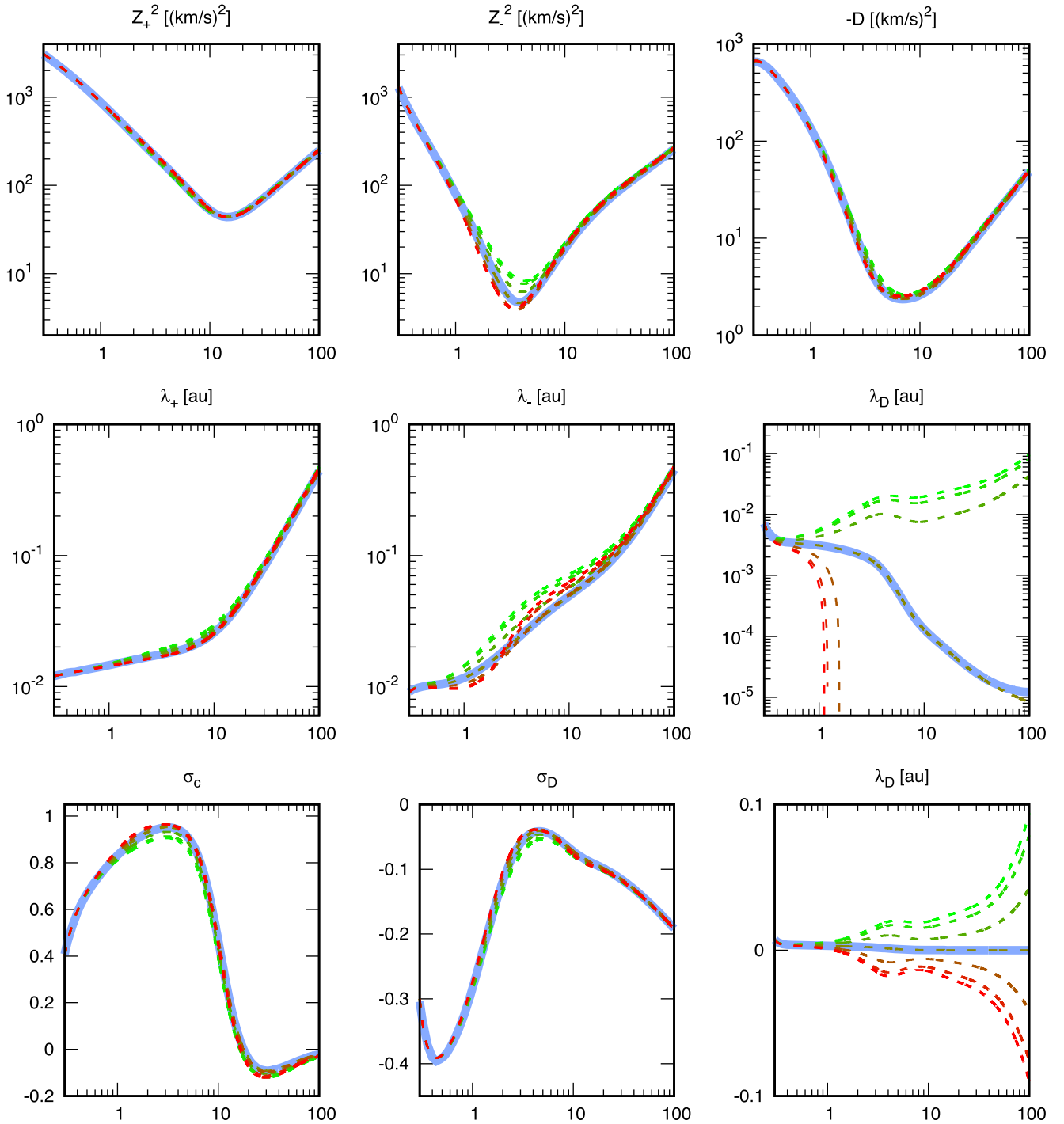
Figure 2. Radial profiles of turbulence quantities $Z_\pm^2$, D, $\lambda_\pm$, λ_D, σ_c, and σ_D as a function of the Sun-centered radial position in au. Dashed curves have been obtained by solving the the 1D set of Equations (44)–(47) for values ranging from $\gamma = 0$ (green) to $\gamma = 90°$ (red) in steps of 15°. The solid thick blue curve, which coincides exactly with the $\gamma = 45°$ 1D radial model curve, shows the time-converged solution obtained from solving the 3D set of Equations (A1)–(A5), subject to boundary conditions as listed in Table 3. As λ_D can be negative, it is shown both with a linear and a logarithmic scaling.

The images for Z^2 reveal substantial magnitude variations and structuring, although these features are much reduced inside the HP. The low ISM levels increase significantly within ~10 au of the HP, and Z^2 tends to be largest near and somewhat inside the HP and toward the TS and further inward. Moreover, inside the HP (and for $r \lesssim 150$ au) the variations with φ and ϑ are relatively weak, except that there is an extended equatorial zone where Z^2 is only a fraction of the polar levels, reminiscent of the solar wind inside the TS. This

correlation between low/high Z^2 and (radial) wind speed is present in the inner boundary conditions and is thus seen to persist out to the HP. Overall this behavior is similar to that obtained with both our three-equation model (Section 2.4) and the Usmanov et al. (2016) model. However, there are certainly differences, as one should expect in view of the refined turbulence modeling, e.g., different length scales for the different turbulence components, and the single-fluid versus multifluid approaches.
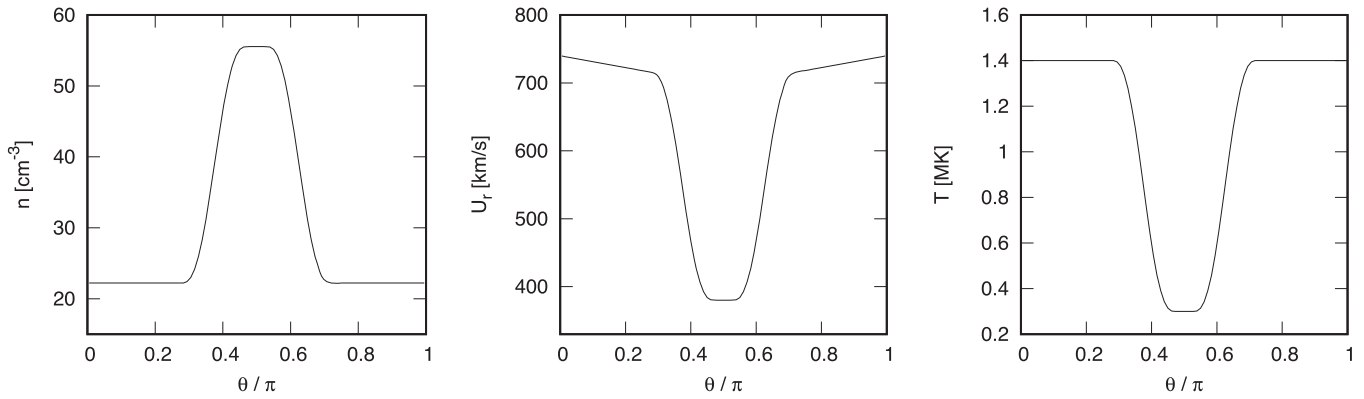
Figure 3. Profiles for number density n (left), radial velocity U_r (middle), and temperature T (right) as a function of the colatitude ϑ as used for the inner boundary conditions at 0.3 au.

The simulated σ_c values found in the IHS are rather small (in fact often consistent with zero and so again consistent with Usmanov et al. 2016), indicating roughly equal amounts of $Z_\pm^2$. Between the HP and the bow shock much higher values of $|\sigma_c|$ are seen, sometimes close to extremal, indicating near dominance of one of Z_+^2 or Z_-^2. One should however keep in mind that the overall turbulence level $\langle Z^2 \rangle$ is typically much lower in these regions. As already noted, because the model equations do not enforce $|\sigma_c| \leqslant 1$, we artificially clamp σ_c within $[-0.98, 0.98]$ to ensure continued numerical computability. In particular, there are regions near the bow shock where the lowest threshold of -0.98 is maintained only by this clamping, even in the converged stationary state. This suggests that future investigations similar to ours but targeting the OHS will need to find ways to self-consistently ensure physically reasonable bounds for σ_c are obeyed.

Regarding σ_D, we see that inside the HP it is negative almost everywhere. In the upwind IHS, σ_D exhibits relatively little variation, typically maintaining values around -0.2 or even closer to zero. Elsewhere, σ_D can be close to its minimum of -1, indicating dominance of magnetic fluctuation energy, as seen on the flanks of the HP. This is further evidence that the simplification $\sigma_D = $ constant (e.g., $-1/3$)—as often used inside the TS and, in particular, also in the only other model studying the turbulence evolution in a "realistic" heliosheath (Usmanov et al. 2016)—is probably inappropriate to use when larger volumes of the heliosphere are considered. This was already found in "inside the TS" studies (Adhikari et al. 2015, 2017; Shiota et al. 2017), as well as for our six-equation model of the inner heliosphere analyzed in Section 3.5.

Beyond the HP, especially in the upwind direction, there are large regions where $\sigma_D > 0$, indicating "excess" fluctuation kinetic energy. The spatial variation of σ_D can be understood as a consequence of the piled-up magnetic field, which, via the Alfvénic speed, decreases the timescale τ_D, thereby making damping locally less efficient. However, as already noted in connection with the σ_c values, one should keep in mind that the turbulence amplitude in these regions is very small and not of any significance to the behavior inside the HP.

Another set of interesting and currently unexplained features are the pronounced regions of low σ_D emanating from both ecliptic triple points and the meridional downwind part of the Mach disk. We note, however, that these could also be an artifact of the one-fluid approach, given that the Mach disk, and hence also the triple point, tends to be more rudimentary or

even completely absent in multifluid models of the global heliosphere. (For a more general discussion of the Mach disk and the associated triple points, see, e.g., Scherer et al. 2020).

Finally, the new six-equation model also allows the consideration of L_D and the Elsässer length scales, $\lambda_\pm$, separately and in detail for the entire heliosphere and the local ISM. This extends other studies in which these three quantities were also distinguished (Adhikari et al. 2015, 2017; Shiota et al. 2017). In those earlier works, however, the computational domain was restricted to lie well inside the TS and be either spherically symmetric with only radial variations, or support latitudinal variations but with the outer boundary at 6 au.

Roughly speaking, L_D is tiny in the ISM ahead of the bow shock, and larger, although still small compared to $L_\pm$, around and inside the HP. Sunward of the bow shock, $\lambda_\pm$ tend to increase with the heliocentric distance and to be the largest (~ 10 au) between the bow shock and the HP. As it might have been anticipated for regions with $\sigma_c \approx 0$, inside the HP $\lambda_+ \approx \lambda_-$. For a given r inside the HP, the Elsässer length scales do not vary strongly with either φ or ϑ.

We have also performed simulations with substantially different outer (ISM) boundary conditions. For example, using $\lambda_\pm = 1$ au or $Z^2 = 1$ (km s^{-1})^2, respectively, 2000 times smaller and 100 times larger than the values listed in Table 3. Such changes make very little difference to the location of the HP and indicate the weak impact of the ISM fluctuations on the behavior inside the HP.

5. Summary

We have constructed a refined model describing the evolution of (incompressible) turbulence in the entire 3D heliosphere, including the region beyond the TS up to the HP, i.e., in the IHS. The turbulence evolution is self-consistently coupled to the large-scale solar wind and the ISM, with these evolved using compressible one-fluid 3D MHD.

In this first generalization, with respect to the turbulence description, of the approach employed by Usmanov et al. (2016) several extensions have been implemented. In addition to following the Elsässer energies, we have (i) allowed the residual energy to self-consistently evolve instead of keeping it at the "traditional" value of $-1/3$ and (ii) allowed for distinct length scales for each of these three quantities. While the nonlinear effects in the equations for the Elsässer energies and their length scales are implemented using well-known von Kármán–Howarth style modeling of homogeneous MHD
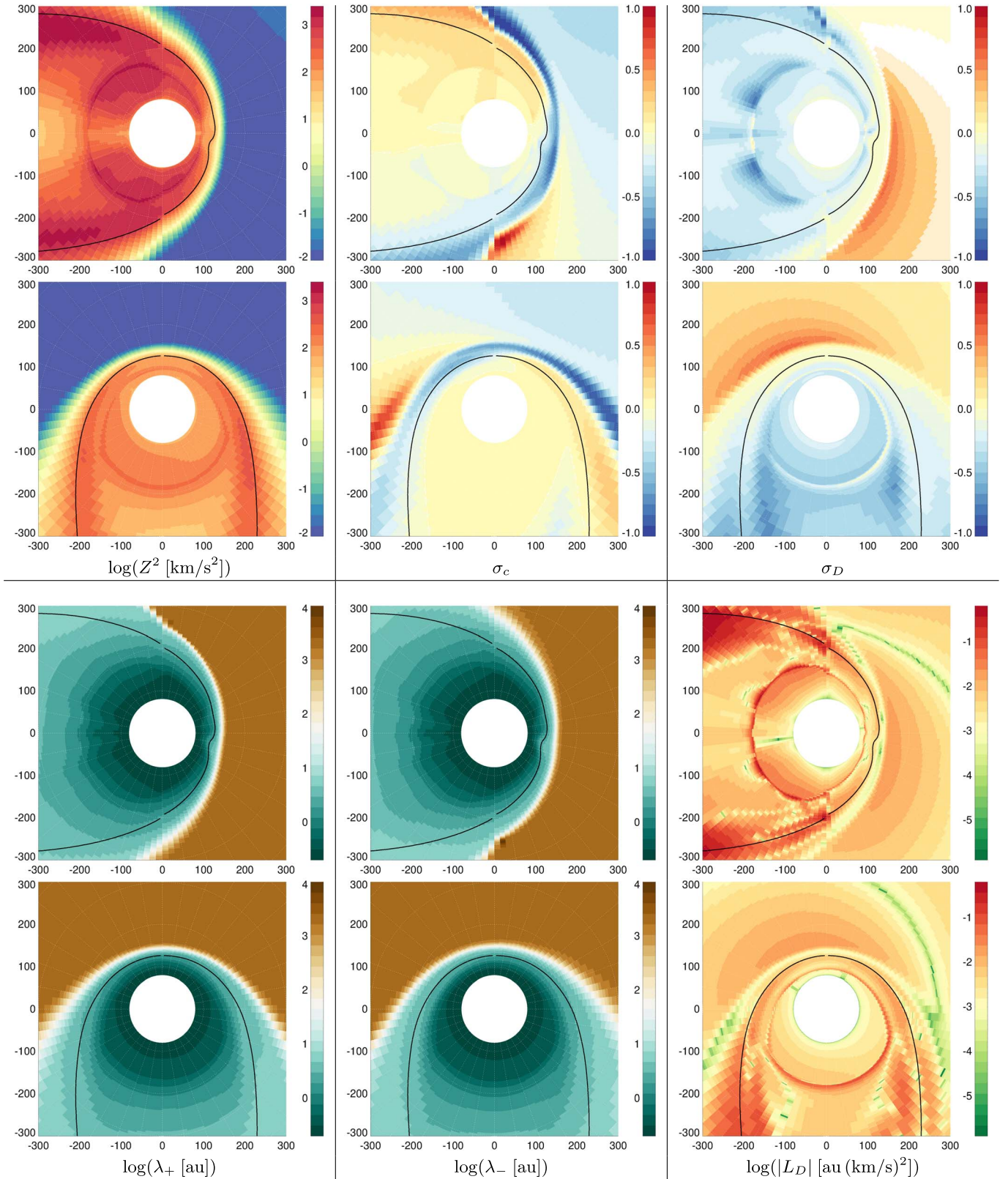
Figure 4. Turbulence quantities Z^2, σ_c, σ_D, $\lambda_\pm$, and $|L_D|$. In each case, the top panel (rows 1 and 3) shows a meridional ($\varphi = 0$) cut through the computational domain, and the bottom panel the corresponding equatorial ($\vartheta = \pi/2$) cut. White circles indicate the computational inner boundary (80 au), and the thick black lines mark the HP. In the σ_c and σ_D plots dashed lines indicate zero-level contours. The position of the TS is seen most clearly in the σ_D and L_D panels. The bow shock lies outside the shown regions; in the upwind direction it is at $r \approx 400$ au.

turbulence, the energy difference (not conserved in the absence of dissipation) and its length scale are modeled using distinct phenomenological approaches. In particular, for both D and L_D

we invoke damping toward zero on an Alfvénic timescale (due to the Alfvén effect) and for D employ an additional always negative "source" term associated with the energy cascade rate.

Another difference to earlier modeling approaches concerns the local turbulence geometry. We clarified the impact of the choice of measurement direction $\hat{\boldsymbol{n}}$ for correlation functions associated with 2D fluctuations in transport models and introduced a coordinate-independent description via an averaging procedure.

We have, first, related the quantitative findings obtained with the resulting six-equation model to those of previous studies as well as to observational data provided therein. While for the supersonic solar wind region, to which those studies were limited, we found some differences in radial profiles—mainly as a consequence of the differences in the turbulence modeling —our results appear to be compatible with the spacecraft data.

Second, after this validation, we illustrated and studied the solutions of the resulting six-equation model for the three-dimensionally structured outer heliosphere in detail. For the Elsässer energies and their length scales we predict behavior that is similar to that found by Usmanov et al. (2016) and for the cross helicity we also obtain rather low values. For the newly computed nonconstant residual energy we predict values mostly below zero in the IHS. In the upwind IHS typical values of σ_D are around -0.15, while at the flanks of the HP they decrease close to the minimum possible value of -1, indicating a dominance of magnetic fluctuations there. These deviations from the often used value of $-1/3$ make it obvious that the latter approximation is difficult to justify for the IHS. Finally,

in the IHS the associated length scale (λ_D) remains significantly shorter than those of the Elsässer energies.

We anticipate that the presented model and its predictions may be of use in other space and astrophysics applications. For example, it may serve as a basis for future analogously refined modeling of the main transport parameters of cosmic rays in the outer heliosphere. Their spatial diffusion and drift both depend on the fluctuation levels of the various turbulence components as is discussed and quantitatively illustrated in, e.g., Wiengarten et al. (2016). In particular, the variation in the residual energy D (or, equivalently, in the Alfvén ratio) can be expected to have a significant impact. Future activities should also comprise a self-consistent incorporation of compressible fluctuations as well as an investigation of the effects of disturbances propagating through the IHS.

Appendix A
Conservative Form of the Six-equation Model

Here we list the γ-averaged versions of the turbulence transport Equations (23)–(26) in conservative form, using Z^2 and H_c instead of $Z_\pm^2$. This form has the advantage that the only gradients of turbulence variables that need to be evaluated are the divergences on the left hand sides of each equation. Additionally, the identities expressed in Equations (29) and (30) have been used, enabling elimination of all occurrences of $\langle \Sigma(\boldsymbol{U}) \rangle_\gamma$ and $\langle \Sigma(\boldsymbol{B}) \rangle_\gamma$ after use of Equation (39). In Equations (A1) and (A4), the final term involves the Heaviside step function $H(\,\cdot\,)$, which acts to restrict the pickup ion driving to the region inside the HP:

$$\frac{\partial Z^2}{\partial t} + \nabla \cdot [Z^2\,\boldsymbol{U} - H_c\boldsymbol{V}_A] = \frac{Z^2 - D}{2}(\nabla \cdot \boldsymbol{U}) - 2H_c(\nabla \cdot \boldsymbol{V}_A) + D\,\Gamma(\boldsymbol{U}) - \frac{q_+ + q_-}{2} + \dot{E}_{\mathrm{pui}}H(-\Psi), \tag{A1}$$

$$\frac{\partial H_c}{\partial t} + \nabla \cdot [H_c\,\boldsymbol{U} - Z^2\boldsymbol{V}_A] = \frac{H_c}{2}(\nabla \cdot \boldsymbol{U}) - 2Z^2(\nabla \cdot \boldsymbol{V}_A) + D\,\Gamma(\boldsymbol{V}_A) - \frac{q_+ - q_-}{2}, \tag{A2}$$

$$\frac{\partial D}{\partial t} + \nabla \cdot [D\,\boldsymbol{U}] = \frac{D - Z^2}{2}(\nabla \cdot \boldsymbol{U}) + Z^2\,\Gamma(\boldsymbol{U}) - H_c\Gamma(\boldsymbol{V}_A) - \alpha_D\frac{D}{\tau_D} - \frac{q_+ + q_-}{2}, \tag{A3}$$

$$\frac{\partial L_\pm}{\partial t} + \nabla \cdot [L_\pm(\boldsymbol{U} \mp \boldsymbol{V}_A)] = \frac{L_\pm - L_D}{2}(\nabla \cdot \boldsymbol{U}) \mp 2L_\pm(\nabla \cdot \boldsymbol{V}_A) + L_D[\Gamma(\boldsymbol{U}) \pm \Gamma(\boldsymbol{V}_A)]$$
$$+ (\beta - \alpha)Z_\pm^2 Z_\mp + \frac{L_\pm\,\dot{E}_{\mathrm{PI}}}{Z^2 \pm H_c}H(-\Psi), \tag{A4}$$

$$\frac{\partial L_D}{\partial t} + \nabla \cdot [L_D\,\boldsymbol{U}] = \frac{2L_D - L_+ - L_-}{4}(\nabla \cdot \boldsymbol{U}) + \frac{L_+ + L_-}{2}\,\Gamma(\boldsymbol{U}) - \frac{L_+ - L_-}{2}\,\Gamma(\boldsymbol{V}_A) - \frac{L_D}{\tau_D}. \tag{A5}$$

Appendix B
Special Case: Reduction to a Single-length-scale Model

Under appropriate conditions the six-equation transport model reduces to the three-equation model of Section 2.2; see the paragraph following Equation (30). The ensuing equation for the single length scale $\lambda\,(=\lambda_+ = \lambda_- = \lambda_D)$, Equation (13), is repeated

here for convenient reference,

$$\frac{\partial \lambda}{\partial t} + \boldsymbol{U} \cdot \nabla \lambda \underbrace{- \sigma_c \boldsymbol{V}_A \cdot \nabla \lambda}_{\text{crosshelicity}} \underbrace{- \lambda \sigma_D [\nabla \cdot \boldsymbol{U} - 2\Sigma(\boldsymbol{U}) - \Gamma(\boldsymbol{U})]}_{\text{mixing}} = \beta Z f^+(\sigma_c) - \frac{\beta \lambda}{\alpha Z^2} \dot{E}_{\text{pui}}. \tag{B1}$$

This is present implicitly in Matthaeus et al. (1994) and is essentially Equation (10) in Wiengarten et al. (2016), after setting their wave-like component to zero for comparison with a single-component model (and with allowance for notation changes). See also Matthaeus et al. (1996). However, in some works the full Equation (B1) has not been employed, with one or both of the underbracketed terms missing. Here we discuss some reasons why these terms might be absent.

The first of these terms, $-\sigma_c \boldsymbol{V}_A \cdot \nabla \lambda$, arises in connection with linear transport effects. Its form is independent of any specific modeling approach associated with imposed or approximated fluctuation symmetries (e.g., structural similarity, exact tensor structure). Thus, we argue that it should in general be present when terms of $O(V_A)$ are retained. Some single-length-scale SW transport models that retain many of the $O(V_A)$ terms nonetheless omit the $O(V_A)$ term of Equation (B1) from their length scale evolution equation (e.g., Zank et al. 2012a; Wiengarten et al. 2015; Usmanov et al. 2016).

Papers that lack the term labeled "mixing" appear to do so because of assumptions or errors connected with the structural similarity approximation. To illustrate consider a correlation tensor $R_{ij}(\boldsymbol{\zeta}) = \langle v_i(\boldsymbol{x}) v_j(\boldsymbol{x} + \boldsymbol{\zeta}) \rangle$, with $\boldsymbol{\zeta}$ being the vector lag. The direction of $\boldsymbol{\zeta}$ is unrestricted, although for a specific symmetry of the turbulence (e.g., 2D) some directions may not provide much information.

In general, the tensor structures of (i) the *variance* matrix $R_{ij}(0)$ and (ii) the lag-integrated correlation tensor $L_{ij}(\hat{\boldsymbol{\zeta}}) = \int_0^\infty R_{ij}(\zeta)\,d\zeta$ differ, and in particular they do so for both isotropic turbulence and axisymmetric 2D turbulence (Batchelor 1970; Matthaeus et al. 1994). This was incorrectly accounted for in Breech et al. (2008) with an error associated with integration of their Equation (17) causing complete (but erroneous) cancellation of the mixing terms in their λ equation;[11] the equations for Z^2 and H_c were unaffected by the error. Unfortunately this omission propagated into some later papers (e.g., Oughton et al. 2011; Usmanov et al. 2011, 2016). A related issue arises in Zank et al. (2012a), who employed a structural similarity approach to approximate both $R_{ij}(0)$ and L_{ij} as being proportional to $\delta_{ij} - \hat{n}_i \hat{n}_j$, for a suitable choice of the unit vector $\hat{\boldsymbol{n}}$. This is problematic in that the tensor structures of $R_{ij}(0)$ and L_{ij} are then the same, rather than different (assuming the same $\hat{\boldsymbol{n}}$ is used in both). With their choices for the proportionality constants, this approach also leads to cancellation of the mixing terms in (their equivalent of) Equation (B1). The same issue is present in Wiengarten et al. 2015.

Note that it is possible for the mixing term in Equation (B1) to vanish because of an "internal cancellation" of its contributing pieces. For example, when the large-scale SW speed is approximated as uniform and constant, i.e., $\boldsymbol{U} = U\hat{\boldsymbol{r}}$—as considered in, e.g., Breech et al. (2008), Adhikari et al. (2015), and Section 3.5—this mixing term is

$$+\lambda \sigma_D \frac{U}{r} [\sin^2 \psi - 2(\hat{\boldsymbol{n}} \cdot \hat{\boldsymbol{r}})^2] = \lambda \sigma_D \frac{U}{r} [1 - 2\sin^2 \gamma] \sin^2 \psi. \tag{B2}$$

This is zero when $\gamma = \pi/4$; see Equation (34). For general SW velocities the mixing term can be made to vanish by averaging Equation (B1) over all angles γ (i.e., over all directions $\hat{\boldsymbol{n}} \perp \boldsymbol{B}$). See Section 3.3 and Equation (39) in particular.

ORCID iDs

Jens Kleimann https://orcid.org/0000-0001-6122-9376
Sean Oughton https://orcid.org/0000-0002-2814-7288
Horst Fichtner https://orcid.org/0000-0002-9151-5127
Klaus Scherer https://orcid.org/0000-0002-9530-1396

References

Adhikari, L., Zank, G. P., Bruno, R., et al. 2015, ApJ, 805, 63
Adhikari, L., Zank, G. P., Hunana, P., et al. 2017, ApJ, 841, 85
Alexashov, D., & Izmodenov, V. 2005, A&A, 439, 1171
Balsara, D. S., & Spicer, D. 1999, JCoPh, 148, 133
Bandyopadhyay, R., Matthaeus, W. H., Oughton, S., & Wan, M. 2019, JFM, 876, 5
Bandyopadhyay, R., Oughton, S., Wan, M., et al. 2018, PhRvX, 8, 041052
Batchelor, G. K. 1970, The Theory of Homogeneous Turbulence (Cambridge: Cambridge Univ. Press)
Bavassano, B., Pietropaolo, E., & Bruno, R. 2001, JGR, 106, 10659
Bieber, J. W., Evenson, P. A., & Matthaeus, W. H. 1987, ApJ, 315, 700
Bigot, B., & Galtier, S. 2011, PhRvE, 83, 026405
Bigot, B., Galtier, S., & Politano, H. 2008, PhRvE, 78, 066301
Breech, B., Matthaeus, W. H., Minnie, J., et al. 2008, JGR, 113, A08105

Bruno, R. 2019, E&SS, 6, 656
Burlaga, L. F., Florinski, V., & Ness, N. F. 2018, ApJ, 854, 20
Burlaga, L. F., Ness, N. F., & Acuña, M. H. 2006, ApJ, 642, 584
Chen, C. H. K., Bale, S. D., Bonnell, J. W., et al. 2020, ApJS, 246, 53
Dosch, A., Adhikari, L., & Zank, G. P. 2013, in AIP Conf. Proc. 1539, Solar Wind 13, ed. G. P. Zank et al. (Melville, NY: AIP), 155
Engelbrecht, N. E., & Burger, R. A. 2013, ApJ, 772, 46
Fichtner, H., Kleimann, J., Yoon, P. H., et al. 2020, ApJ, 901, 76
Fraternale, F., Adhikari, L., Fichtner, H., et al. 2022, SSRv, 218, 50
Fraternale, F., & Pogorelov, N. V. 2021, ApJ, 906, 75
Fraternale, F., Pogorelov, N. V., Richardson, J. D., & Tordella, D. 2019, ApJ, 872, 40
Grappin, R., Müller, W.-C., & Verdini, A. 2016, A&A, 589, A131
Grappin, R., Pouquet, A., & Léorat, J. 1983, A&A, 126, 51
Hossain, M., Gray, P. C., Pontius, D. H., Jr., Matthaeus, W. H., & Oughton, S. 1995, PhFl, 7, 2886
Isenberg, P. A., Smith, C. W., & Matthaeus, W. H. 2003, ApJ, 592, 564
Kissmann, R., Kleimann, J., Krebl, B., & Wiengarten, T. 2018, ApJS, 236, 53
Kraichnan, R. H. 1965, PhFl, 8, 1385
Larrodera, C., & Cid, C. 2020, A&A, 635, A44
Linkmann, M., Berera, A., & Goldstraw, E. E. 2017, PhRvE, 95, 013102
Mangeney, A., Grappin, R., & Velli, M. 1991, in Advances in Solar System Magnetohydrodynamics, ed. E. R. Priest & A. W. Hood (Cambridge: Cambridge Univ. Press), 327
Marsch, E., & Richter, A. K. 1984, JGR, 89, 5386

---

[11] The $O(V_A)$ term is also absent; however this is consistent as their model neglects all such terms.

Marsch, E., & Tu, C.-Y. 1989, JPlPh, 41, 479
Matthaeus, W. H., Goldstein, M. L., & Roberts, D. A. 1990, JGR, 95, 20673
Matthaeus, W. H., Minnie, J., Breech, B., et al. 2004, GeoRL, 31, 12803
Matthaeus, W. H., Oughton, S., Pontius, D. H., Jr., & Zhou, Y. 1994, JGR, 99, 19267
Matthaeus, W. H., Zank, G. P., & Oughton, S. 1996, JPlPh, 56, 659
Matthaeus, W. H., Zank, G. P., Smith, C. W., & Oughton, S. 1999, PhRvL, 82, 3444
McComas, D. J., Barraclough, B. L., Funsten, H. O., et al. 2000, JGR, 105, 10419
Müller, W.-C., & Grappin, R. 2005, PhRvL, 95, 114502
Oughton, S., Dmitruk, P., & Matthaeus, W. H. 2006, PhPl, 13, 042306
Oughton, S., & Engelbrecht, N. E. 2021, NewA, 83, 101507
Oughton, S., Matthaeus, W. H., Smith, C. W., Breech, B., & Isenberg, P. A. 2011, JGR, 116, A08105
Oughton, S., Matthaeus, W. H., Wan, M., & Parashar, T. N. 2016, JGR, 121, 5041
Oughton, S., Priest, E. R., & Matthaeus, W. H. 1994, JFM, 280, 95
Oughton, S., Rädler, K.-H., & Matthaeus, W. H. 1997, PhRvE, 56, 2875
Parker, E. N. 1958, ApJ, 128, 664
Perri, S., & Balogh, A. 2010, GeoRL, 37, L17102
Petrukovich, A. A., Malova, H. V., Popov, V. Y., et al. 2020, PhyU, 63, 801
Pogorelov, N. V., Fichtner, H., Czechowski, A., et al. 2017, SSRv, 212, 193
Pogorelov, N. V., Suess, S. T., Borovikov, S. N., et al. 2013, ApJ, 772, 2
Pouquet, A., Frisch, U., & Léorat, J. 1976, JFM, 77, 321
Richardson, I. G. 2018, LRSP, 15, 1
Richardson, J. D., & Burlaga, L. F. 2013, SSRv, 176, 217
Roberts, D. A., Klein, L. W., Goldstein, M. L., & Matthaeus, W. H. 1987, JGR, 92, 11021
Roy, S., Chhiber, R., Dasso, S., Ruiz, M. E., & Matthaeus, W. H. 2022, PhRvE, 105, 045204
Scherer, K., Baalmann, L. R., Fichtner, H., et al. 2020, MNRAS, 493, 4172
Scherer, K., Ferreira, S., Potgieter, M., & Fichtner, H. 2006, in AIP Conf. Proc. 858, Physics of the Inner Heliosheath: Voyager Observations, Theory, and Future Prospects (Melville, NY: AIP), 20
Shiota, D., Zank, G. P., Adhikari, L., et al. 2017, ApJ, 837, 75
Smith, C. W., Matthaeus, W. H., Zank, G. P., et al. 2001, JGR, 106, 8253
Tennekes, H., & Lumley, J. L. 1972, First Course in Turbulence (Cambridge MA: MIT Press)
Tu, C.-Y., Marsch, E., & Thieme, K. M. 1989, JGR, 94, 11739
Usmanov, A. V., Goldstein, M. L., & Matthaeus, W. H. 2014, ApJ, 788, 43
Usmanov, A. V., Goldstein, M. L., & Matthaeus, W. H. 2016, ApJ, 820, 17
Usmanov, A. V., Matthaeus, W. H., Breech, B. A., & Goldstein, M. L. 2011, ApJ, 727, 84
Verscharen, D., Klein, K. G., & Maruca, B. A. 2019, LRSP, 16, 5
Wan, M., Oughton, S., Servidio, S., & Matthaeus, W. H. 2012, JFM, 697, 296
Wiengarten, T., Fichtner, H., Kleimann, J., & Kissmann, R. 2015, ApJ, 805, 155
Wiengarten, T., Oughton, S., Engelbrecht, N. E., et al. 2016, ApJ, 833, 17
Williams, L. L., & Zank, G. P. 1994, JGR, 99, 19229
Yokoi, N. 2006, PhPl, 13, 062306
Yokoi, N., & Hamba, F. 2007, PhPl, 14, 112904
Yokoi, N., Rubinstein, R., Yoshizawa, A., & Hamba, F. 2008, JTurb, 9, N37
Zank, G. P., Adhikari, L., Hunana, P., et al. 2017, ApJ, 835, 147
Zank, G. P., Dosch, A., Hunana, P., et al. 2012a, ApJ, 745, 35
Zank, G. P., Jetha, N., Hu, Q., & Hunana, P. 2012b, ApJ, 756, 21
Zank, G. P., Matthaeus, W. H., & Smith, C. W. 1996, JGR, 101, 17093
Zhou, Y., & Matthaeus, W. H. 1990, JGR, 95, 10291